Supplementary Materials

Evidence for single variant in altermagnetic RuO_2(101) thin films

Cong He,[1,§,#] Zhenchao Wen,[1,§,*] Jun Okabayashi,[2,*] Yoshio Miura,[1,3*] Tianyi Ma,[1] Tadakatsu Ohkubo,[1] Takeshi Seki,[4,5] Hiroaki Sukegawa,[1] and Seiji Mitani[1]

[1]National Institute for Materials Science (NIMS), Tsukuba 305-0047, Japan

[2]Research Center for Spectrochemistry, The University of Tokyo, Bunkyo, Tokyo 113-0033, Japan

[3]Faculty of Electrical Engineering and Electronics, Kyoto Institute of Technology, Kyoto 606-8585, Japan

[4]Institute for Materials Research, Tohoku University, Sendai 980-8577, Japan

[5]Center for Science and Innovation in Spintronics, Tohoku University, Sendai 980-8577, Japan

[#]Present address: Hunan University, Changsha 410082, China

[§]These authors contributed equally to this work.

[*] Wen.Zhenchao@nims.go.jp, jun@chem.s.u-tokyo.ac.jp, miura@kit.ac.jp

1. Annealing temperature dependence of surface morphology and crystal structure

Figures S1a-c show the surface morphology of the RuO_2 (30 nm) thin films annealed at T_a = 300 ºC, 500 ºC and 700 ºC, as characterized by atomic force microscopy (AFM). The corresponding average roughness (R_a) and peak-to-valley (P-V) values are summarized in Figures S1d and 1e, respectively. The R_a increases slightly to 0.30 nm as T_a is raised to 600 ºC, and then increases dramatically to 0.54 nm with a P-V value of 5.30 nm. Figures S1f-h display the reflection high-energy electron diffraction (RHEED) patterns for the samples annealed at the above temperatures. Clearly discernible RHEED streaks are observed for each sample. Look further into the details, these streaks become progressively sharper with increasing T_a, indicating the improved crystallinity at higher annealing temperatures.

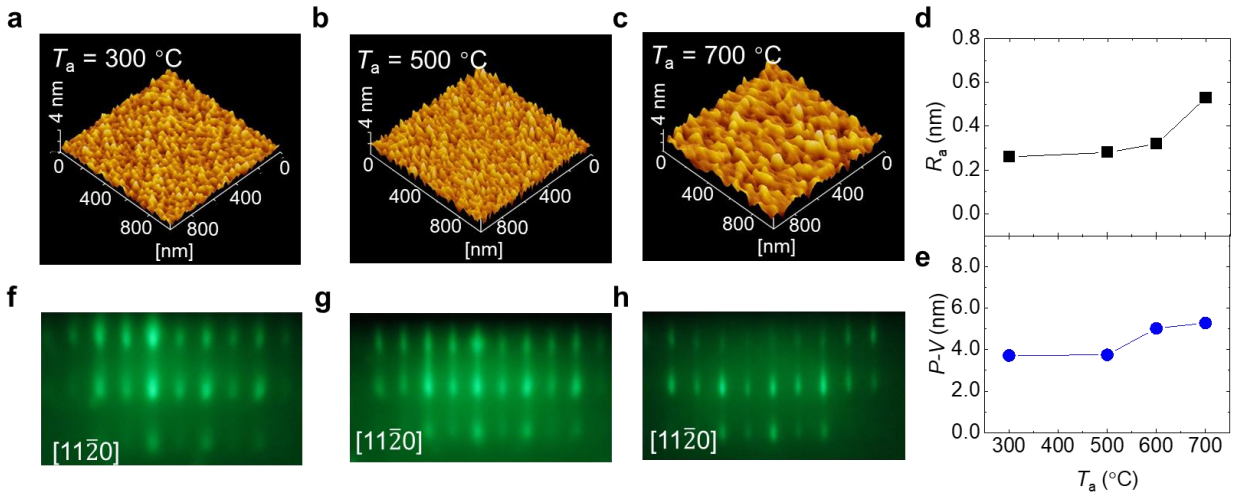

Figure S1. Surface morphology and crystalline structures of RuO_2 thin films. a-c, AFM images of a 30-nm-thick RuO_2 thin film annealed at T_a = 300 ºC, 500 ºC and 700 ºC. **d**, **e**, T_a dependence of R_a and P-V values for the 30-nm-thick RuO_2 sample. **f-h**, RHEED patterns of the RuO_2 thin film at T_a = 300 ºC, 500 ºC and 700 ºC, respectively. The incident electron beam is along the azimuth of $Al_2O_3[11\bar{2}0]$.

2. Transport properties of RuO_2 thin films deposited at various conditions

We prepared RuO_2 thin films on different substrates inlcuding r-plane $Al_2O_3(1\,\bar{1}\,02)$, c-plane $Al_2O_3(0001)$, and MgO(001) substrates with different deposition temperatures and oxygen flow rates. Fig. S2a shows the annealing temperature dependence of conductivity of the RuO_2 thin films for different growth conditions. Note that the unspecified growth conditions are a growth temperature of 300 ºC and an O_2 ratio of 7.7% in Ar and O_2 mixture. We found that the RuO_2 films grown on the $Al_2O_3(1\bar{1}02)$ substrate had the largest conductivity. The conductivity increases as the annealing temperature increases and a maximum conductivity of $2.1 \times 10^6\ \Omega^{-1}m^{-1}$ appeares at an annealing temperature of T_a = 600 ºC. Figure S2b shows the resistivity of the RuO_2 films grown on the $Al_2O_3(1\bar{1}02)$ substrate as a function of measured temperature. It was found that the resistivity decreases with temperature decreases, showing a clear metallic behavior. Figure S2c summarizes the annealing temperature dependence of the residual resistivity as well as the residual-resistance ratio (RRR). The RuO_2 films with high annealing temperatures have small residual resistivities and high RRR, which could be due to the formation of better crystallinity at higher annealing temperatures, in

agreement with the results of xrd and RHEED observations. In addition, we also performed the first-order and second-order differentiation of the curves of resistivity versus measurement temperature to confirm the Néel temperature of the RuO_2 films, as shown in Fig. 1j in main text. the continuity of the differential curves change was clearly observed, which could corresponds to the transition between antiferromagnetic order and paramagnetic order, i.e., the Néel temperature. We found that for the samples annealed at T_a = 600 ºC and 700 ºC, the Néel temperature is around 390 K, comparable to the previous report.[1]

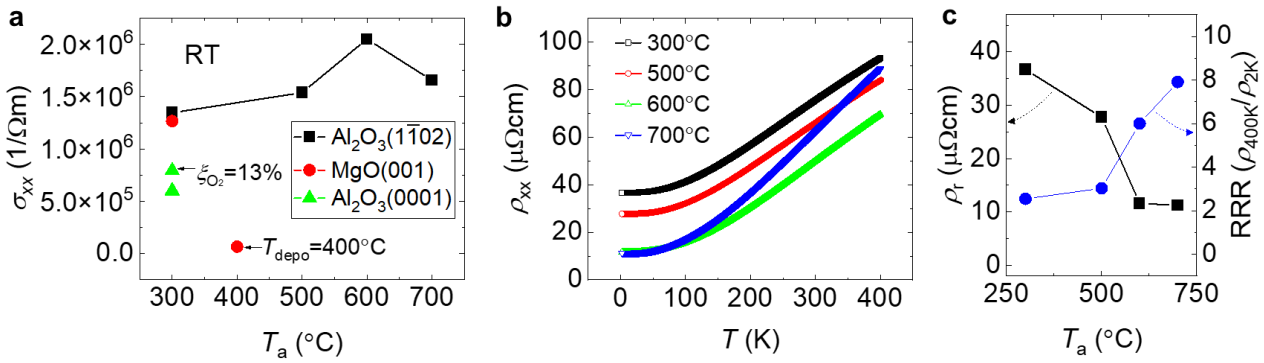

Figure S2. Annealing and measuring temperature dependences of electric transport properties of the RuO_2 thin films deposited at various conditions. a, Conductivity as a function of annealing temperature T_a. for the RuO_2 thin films deposited on different substrates. **b**, Resistivity of RuO_2 thin films deposited on the *r*-plane $Al_2O_3(1\bar{1}02)$ substrates with different T_a. **c**, T_a dependence of residual resistivity and RRR for the $Al_2O_3(1\bar{1}02)$ substrate//RuO_2 (30 nm) thin films.

3. Crystallographic analysis of crystal domains within RuO_2 film

Figure S3 compares the theoretical and experimental scenarios when RuO_2 film is deposited on *r*-plane sapphire $Al_2O_3(1\bar{1}02)$ substrate. Figures S3a and 3c illustrate the lattice matching of $RuO_2(101)$ and $RuO_2(\bar{1}01)$ grown on the $Al_2O_3(1\bar{1}02)$ substrates, respectively. Although these two variants share a mirror relationship, as indicated by the direction of their Néel vectors, no grain boundaries or phase boundaries are detected in our RuO_2 film, as shown in Fig. S3b and Fig. 2b. The experimental HAADF-STEM result is completely consistent with the case of $RuO_2(101)$ grown on $Al_2O_3(1\bar{1}02)$, which verifies the sing-variant growth of $RuO_2(101)$ rather than $RuO_2(\bar{1}01)$.

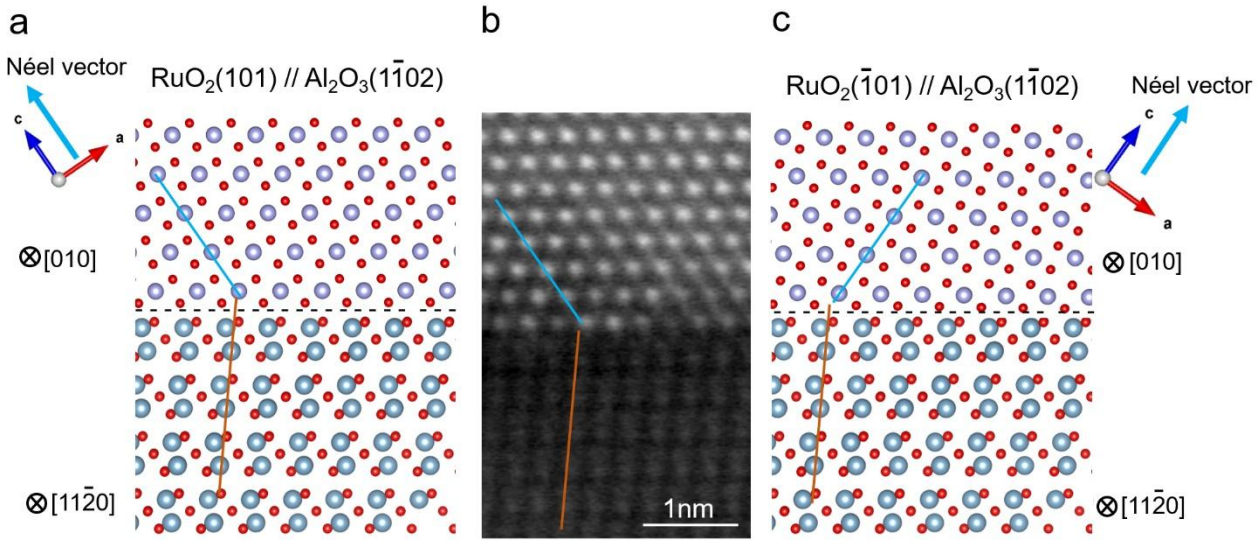

Fig. S3. Crystallographic analysis of crystal domains within RuO_2 film deposited on the *r*-plane $Al_2O_3(1\bar{1}02)$ substrate. **a**, Schematic diagram showing the lattice matching for $RuO_2(101)$ grown on the $Al_2O_3(1\bar{1}02)$ substrate. **b**, HAADF-STEM image showing the direct experimental evidence of RuO_2 film grown on the $Al_2O_3(1\bar{1}02)$ substrate. The light blue arrow represents the direction of Néel vector in RuO_2. **c**, Schematic diagram of the lattice matching between $RuO_2(\bar{1}01)$ and $Al_2O_3(1\bar{1}02)$. The light blue and orange lines in (**a-c**) illustrate the atomic planes in the substrate and the film, respectively.

The low-magnification HAADF-STEM image in Fig. S4a further confirms that no multiple variants formed in the RuO_2 film, i.e. the successful single-variant growth of the film. EDS maps of different elements are shown in Figs. S4b-e. The quantitative line scan profiles in Fig. 4f show that the atomic ratios of O/Al and Ru/O in the substrate and the film are approximately 1.5 and 1.7, respectively. The former value is completely consistent with the stoichiometric ratio of Al_2O_3. The latter, however, is smaller than the theoretical stoichiometric ratio of RuO_2. This may suggest that there are a few O vacancies in the magnetron-sputtered RuO_2 film.

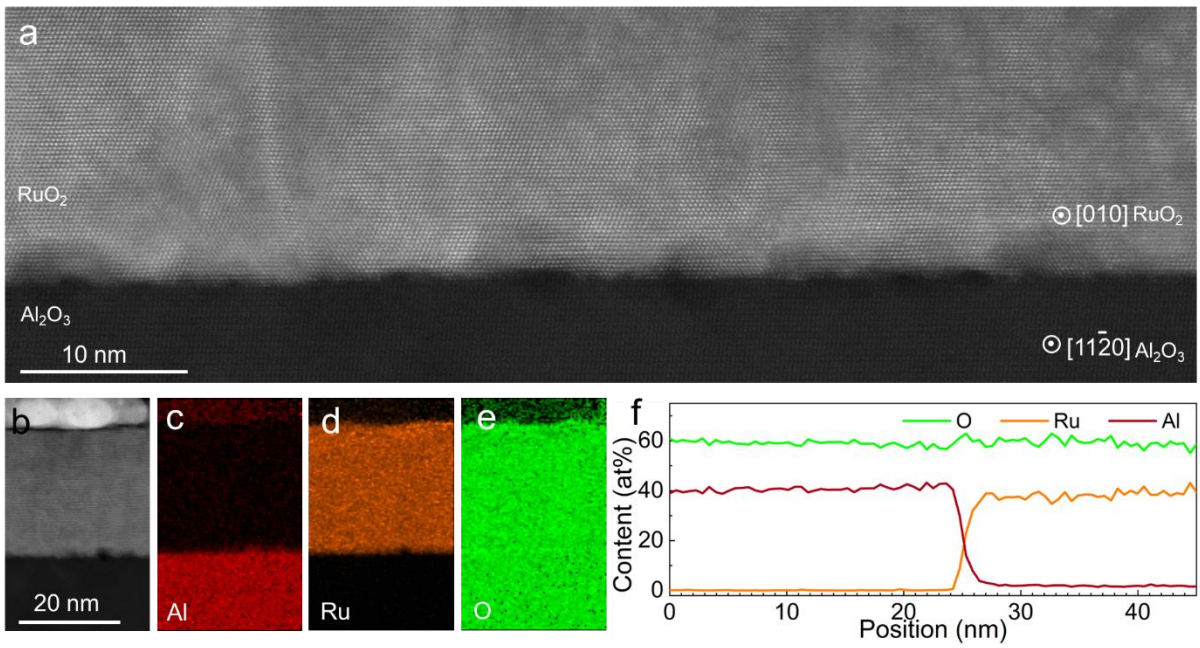

Fig. S4. Chemical composition and O vacancy analyses in the RuO_2 film deposited on the r-plane of substrate, $Al_2O_3(1\bar{1}02)$. a, Low-magnification HAADF-STEM image showing the single-crystalline growth on the *r*-plane $Al_2O_3(1\,\bar{1}\,02)$ substrate, with the electron beam direction of $Al_2O_3(11\bar{2}0)$. **b-e**, EDS mapping analysis of the film. **f**, The quantitative EDS line profiles of elements within the film.

4. The first-principles calculations for surface and variant stability

To clarify the stability of the $Al_2O_3(1\bar{1}02)$ surface, we conducted first-principles density functional theory (DFT) calculations using the VASP-PAW method. We optimized the surface structures of the $Al_2O_3(1\bar{1}02)$ for four different terminations, i.e., Type 1 and Type 2 with O and Al terminations, as shown in Fig. S5a-d. The Type 1 with O termination is corresponding to the $Al_2O_3(1\bar{1}02)$ surface terminated with Al and O ($z = +0.5$) atoms while the Type 2 with O termination is for the $Al_2O_3(1\bar{1}02)$ surface terminated with Al and O ($z = -0.5$) atoms. The calculations reveal that the oxygen-terminated Type 1 surface has the lowest surface energy density shown in Fig. S5 and is the most stable termination. In the experiments, we treated the $Al_2O_3(1\bar{1}02)$ substrates in a muffle furnace at 1000 °C for one hour in an atmospheric environment. This preparation step also supports the formation of a

stable oxygen-terminated surface.

We further calculated the stability of the $RuO_2(101)$ and $RuO_2(\bar{1}01)$ variants by stacking $RuO_2(101)$ and $RuO_2(\bar{1}01)$ cells on the oxygen-terminated Type-1 $Al_2O_3(1\bar{1}02)$ surface, corresponding to Fig. 2f [$Al_2O_3(1\bar{1}02)$/$RuO_2(101)$] and Fig. 2g [$Al_2O_3(1\bar{1}02)$/$RuO_2(\bar{1}01)$] in the manuscript. In these calculations, a supercell containing 162 atoms (Al, O, and Ru) was used, with 4 ML of RuO_2 modeled as either $RuO_2(101)$ or $RuO_2(\bar{1}01)$. After structural relaxation, the cross-sectional atomic distributions in the two cases are shown in Fig. S6. We found that $Al_2O_3(1\bar{1}02)$/$RuO_2(101)$ has a lower total formation energy density by 1.2 J/m^2 compared to $Al_2O_3(1\bar{1}02)$/$RuO_2(\bar{1}01)$. Here, the area density of formation energy is defined as $\gamma_{\text{formation}} = [E_{\text{total}} - (N_{\text{Ru}}\mu_{\text{Ru}} + N_{\text{Al}}\mu_{\text{Al}} + N_{\text{O}}\mu_{\text{O}})]/A$, where N_{Ru}, N_{Al}, and N_{O} are the numbers of Ru, Al and O atoms, μ_{Ru}, μ_{Al}, and μ_{O} are the total energies per atom for bulk hcp-Ru, bulk fcc-Al, and O_2 molecule, and A is the unit cell area of $Al_2O_3(1\bar{1}02)$/$RuO_2(101)$. This result confirms that the $Al_2O_3(1\bar{1}02)$/$RuO_2(101)$ is the more favorable configuration, aligning with experimental observations. Although the interface in the sample's TEM image is not perfectly sharp as a mono-atomic layer, we can find that, across the interface, there are two layers of Al atoms on the atomic terraces of the $Al_2O_3(1\bar{1}02)$ substrate, which is consistent with the Type 1 oxygen-terminated case (Fig. S5a).

Overall, based on the DFT calculations, experimental TEM observations, and substrate preparation process, we conclude that the $Al_2O_3(1\bar{1}02)$ surface is Type 1 with oxygen-termination, allowing the growth of a single-variant $RuO_2(101)$ thin film. The interface structure and energy calculations further support that the $RuO_2(101)$ is a more stable and preferred orientation than $RuO_2(\bar{1}01)$.

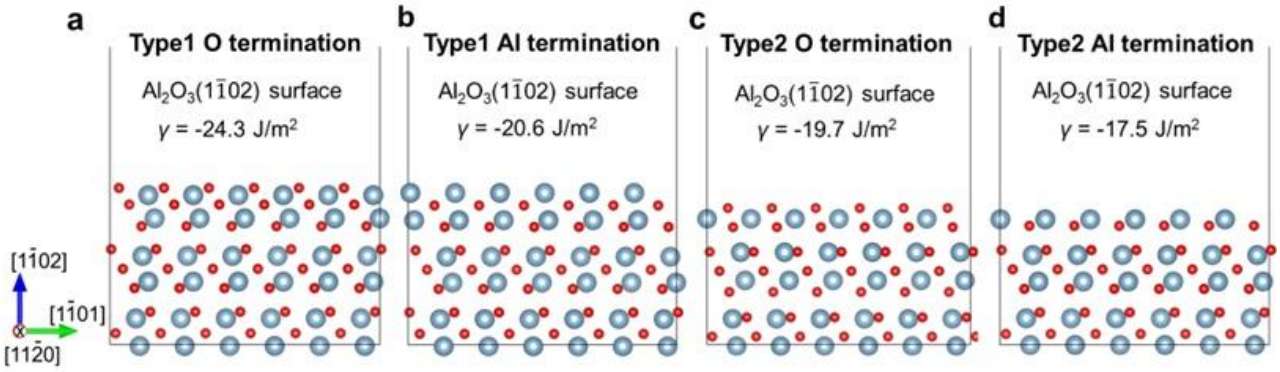

Fig. S5. Illustrations of structures of $Al_2O_3(1\bar{1}02)$ surface. **a**, Type 1 with O termination, **b**, Type 1 with Al termination, **c**, Type 2 with O termination, **d**, Type 2 with Al termination. Red and light blue dots represent oxygen and aluminum atoms, respectively. The formation energy density for each case is also shown.

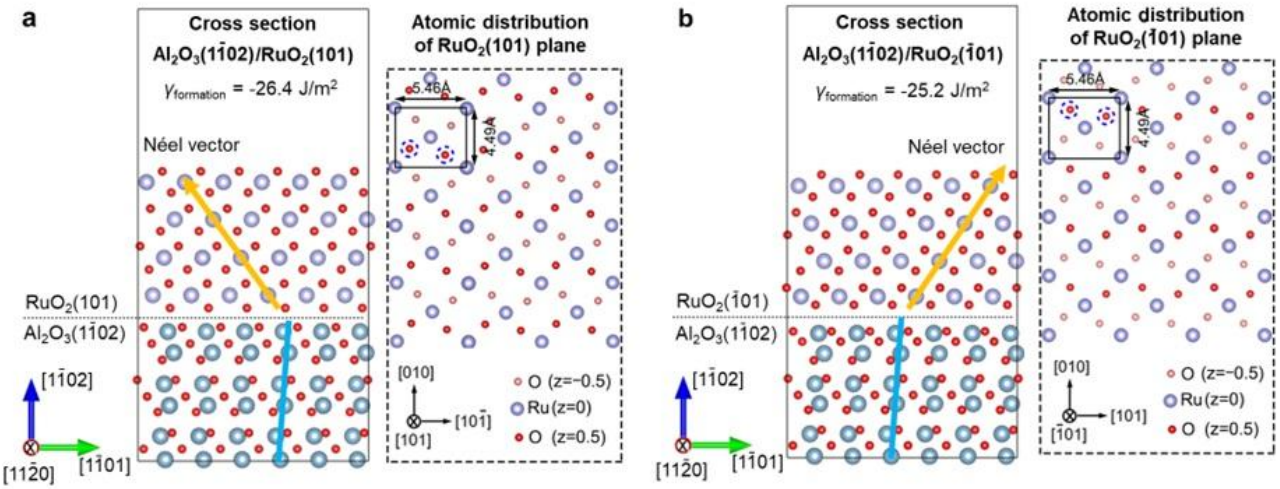

Fig. S6. Illustrations of cross-sectional and in-plane crystal structures and atomic distributions of **a**, $Al_2O_3(1\bar{1}02)/RuO_2(101)$ and **b**, $Al_2O_3(1\bar{1}02)/RuO_2(\bar{1}01)$. Gray dots represent Ru atoms. Red and light blue dots are for oxygen and aluminum atoms, respectively. The formation energy density for each case is also shown.

5. Temperature dependence of XMLD, and integrals of XMLD intensities

Figure S5a displays the temperature-dependent XMLD spectra at 80, 200, 300, and 400 K. The spectra are normalized by XAS intensities. As the temperature increases, the intensity of the XMLD

spectra diminishes, indicating a suppression of magnetic ordering. Given that the Neel temperature is approximately 400 K in RuO_2, the spectra at 400 K arise from the structural contribution, akin to X-ray linear dichroism (XLD). Consequently, we can distinguish between magnetic and structural contributions based on the temperature-dependent measurements. The contribution from the crystalline structure can be roughly estimated at 20% from Fig. S7a.

The integrals of XMLD intensities for M_3 and M_2 edges except for the 3*p* to 4*s* absorption regions are shown Fig. S7b. The XMLD sum rule can be derived as,

$$\langle Q_{zz} \rangle = \frac{l(2l-1)n_h}{2} \frac{\Delta I_{L3}+\Delta I_{L2}}{I_{L3}+I_{L2}}, \qquad \text{(S1)}$$

using the XAS and XMLD intensities of I and ΔI, respectively, for L_2 and L_3 edges.[2,3] Here, in the case of RuO_2, angular quantum number $l = 2$ for 4*d* valence states and $n_h \sim 4$ for Ru^{2+} ($4d^4$) can be adopted. $\langle Q_{zz} \rangle$ is estimated to be the order of 0.01, which results in the charge distribution of 1% order at the Ru sites.

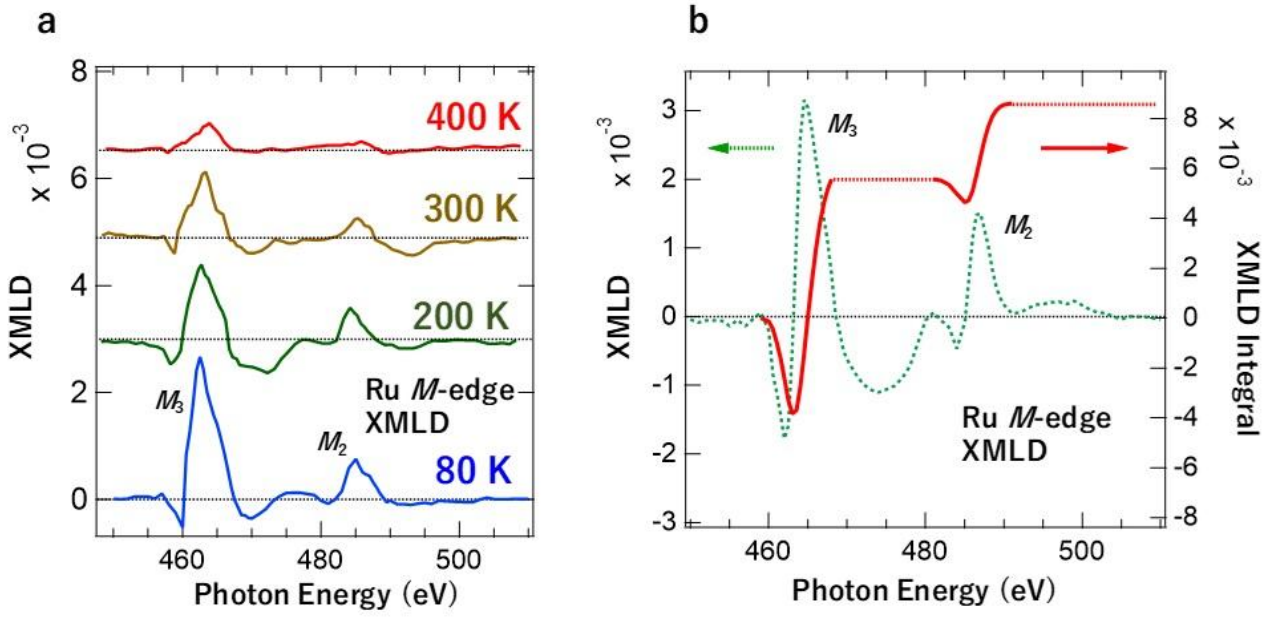

Fig. S7. Analysis of XMLD spectral line shapes. a, XMLD taken at 80, 200, 300, and 400 K. **b**, Integrals of XMLD intensities for M_3 and M_2 edges except for the 3*p* to 4*s* absorption regions.

6. Spin torque ferromagnetic resonance (ST-FMR) measurement in RuO_2(101)/CoFeB bilayers

We performed the ST-FMR measurement[4] to investigate the spin-orbit torques (SOTs) in the RuO_2(5 nm)/CoFeB (2 nm) bilayers deposited on the $Al_2O_3(1\bar{1}02)$ substrate. The film layers were patterned into devices with a rectangular shape separately along the $RuO_2[10\bar{1}]$ and [010] directions with integrated Ta/Au electrodes as coplanar waveguides. Figures S8a and b show the illustrations of RuO_2/CoFeB bilayer structures with applying the charge currents along $RuO_2[10\bar{1}]$ and [010] directions, as well as the generation of spin currents. The magnetic field was applied in plane of the film with the magnitude of 0 ~ 2500 Oe and the in-plane angle φ of 0 ~ 360º. A radio frequency current was applied longitudinally to exert an oscillatory torque to induce precession in the CoFeB layer. This precession causes the device resistance to oscillate through the anisotropic magnetoresistance effect, producing a detectable mixed ST-FMR voltage V that is measured by a lock-in amplifier. The ST-FMR voltage can be fitted by the following equation,[5]

$$V = V_S \frac{\Delta^2}{(H-H_{res})^2+\Delta^2} + V_A \frac{\Delta(H-H_{res})}{(H-H_{res})^2+\Delta^2} \qquad (S2)$$

where Δ is the resonance line width and H_{res} is the resonance field. V_S and V_A correspond to the contributions of the damping-like (DL) and field-like (FL) SOTs. Typical FMR spectra for the RuO_2/CoFeB samples measured at φ = 45° and frequency f = 8 GHz are shown in Figs. S6**c**, **d**. The fitting results using Eq. (S2) are also shown, and the symmetric V_S and antisymmetric V_A contributions of the Lorentzian line shapes of V are separated. The in-plane angle φ dependence of the ST-FMR signal was investigated, and the variations of the V_S and V_A components with respect to φ are shown in Figs. S8 **e**-**h**. The DL and FL torques of *x*-, *y*-, and *z*-polarized spin currents can be separated from the angular dependence of V_S and V_A using the following equations,[6,7]

$$V_S(\varphi) \propto \sin 2\varphi[\tau_x^{DL}\sin\varphi + \tau_y^{DL}\cos\varphi + \tau_z^{FL}] , \qquad (S3)$$

$$V_A(\varphi) \propto \sin 2\varphi[\tau_x^{FL}\sin\varphi + \tau_y^{FL}\cos\varphi + \tau_z^{DL}] . \qquad (S4)$$

Here τ_i^{DL} and τ_i^{FL} are the amplitudes of the DL and FL torques, respectively, where the i indicates the x-, y-, and z-components of the spin currents. The fitting results of the angular dependence of the V_A and V_S of the ST-FMR signal are shown in Figs. S8**e**-**h**. It is found that for the device with the charge current flowing along the $RuO_2[10\bar{1}]$ direction, $\sin 2\varphi \times \cos\varphi$ dominates the fitting result, indicating that the torque originates mainly from spin current polarized in the y-direction, i.e., $RuO_2[010]$ direction. However, for the device with the charge current flowing along the $RuO_2[010]$ direction, the value of τ_z^{DL} is much larger than that of τ_y^{DL}, indicating the generation of tilted spin currents.

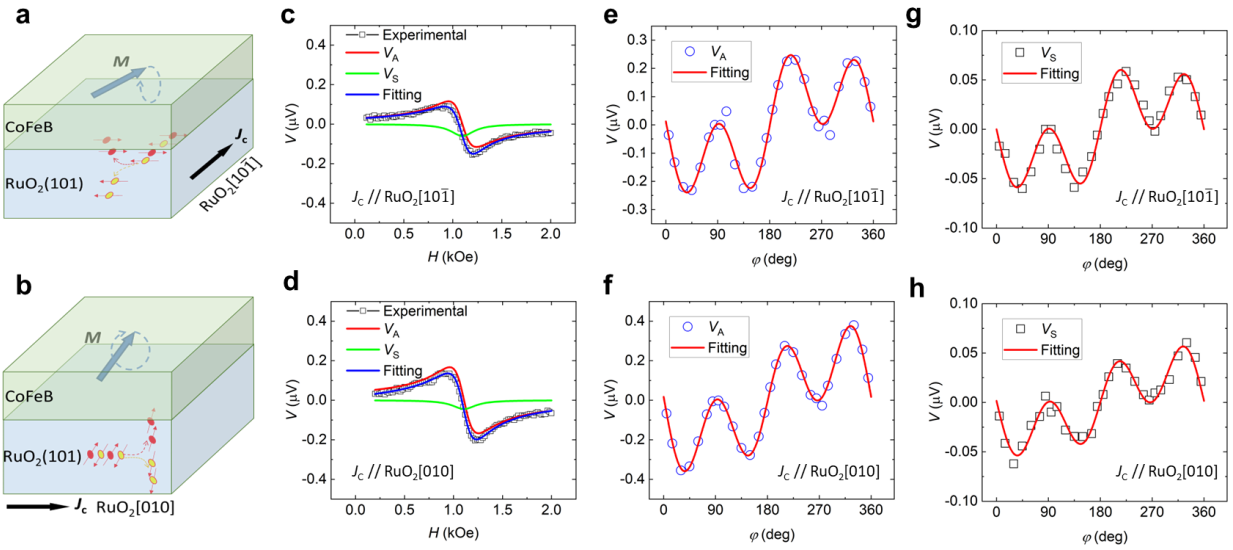

Fig. S8. ST-FMR measurements with the charge current along the [10$\bar{1}$] and [010] directions. a, **b,** Schematic illustrations of RuO_2(101)/CoFeB bilayer structures and spin current generation for the ST-FMR measurements with the charge current along the (**a**) [10$\bar{1}$] and (**b**) [010] directions, respectively. **c**, **d,** Typical ST-FMR spectra with fitting and the separation of antisymmetric (V_A) and symmetric (V_S) components. **e, f**, Antisymmetric voltage amplitudes depending on the angle of in-plane magnetic field. **g, h**, Symmetric component of voltage amplitudes as a function of in-plane magnetic field angle. Red solid lines are the fits using Eqs. (S3) and (S4). **c, e, g** are the results with the measurement configuration shown in (**a**), while **d, f, h** are with the configuration shown in (**b**).

References:

1. Feng, Z. *et al.* An anomalous Hall effect in altermagnetic ruthenium dioxide. *Nat. Electron.* **5**, 735–743 (2022).
2. Okabayashi, J., Iida, Y., Xiang, Q., Sukegawa, H. & Mitani, S. Perpendicular orbital and quadrupole anisotropies at Fe/MgO interfaces detected by x-ray magnetic circular and linear dichroisms. *Appl. Phys. Lett.* **115**, 252402 (2019).
3. Carra, P., König, H., Thole, B. T. & Altarelli, M. Magnetic X-ray dichroism: General features of dipolar and quadrupolar spectra. *Physica B* **192**, 182–190 (1993).
4. Liu, L., Moriyama, T., Ralph, D. C. & Buhrman, R. A. Spin-Torque Ferromagnetic Resonance Induced by the Spin Hall Effect. *Phys. Rev. Lett.* **106**, 036601 (2011).
5. Karimeddiny, S. & Ralph, D. C. Resolving Discrepancies in Spin-Torque Ferromagnetic Resonance Measurements: Lineshape versus Linewidth Analyses. *Phys. Rev. Appl.* **15**, 064017 (2021).
6. MacNeill, D. *et al.* Control of spin–orbit torques through crystal symmetry in WTe2/ferromagnet bilayers. *Nat. Phys.* **13**, 300–305 (2017).
7. Karube, S. *et al.* Observation of Spin-Splitter Torque in Collinear Antiferromagnetic RuO2. *Phys. Rev. Lett.* **129**, 137201 (2022).